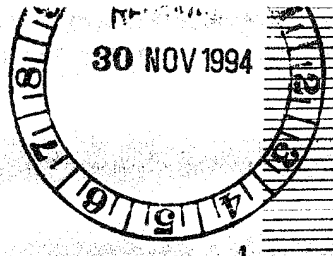

4011

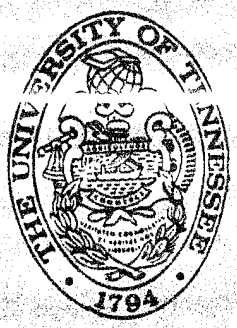

ULTIPLEXED LASER INDUCED FLUORESCEI NON-EQUILIBRIUM PROCESSES IN ARCJ

Dennis Keefer

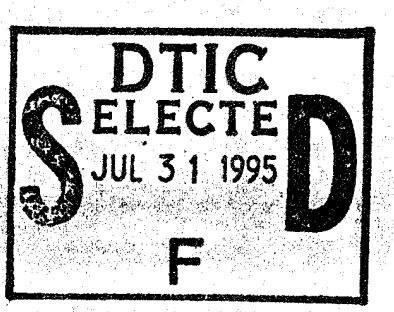

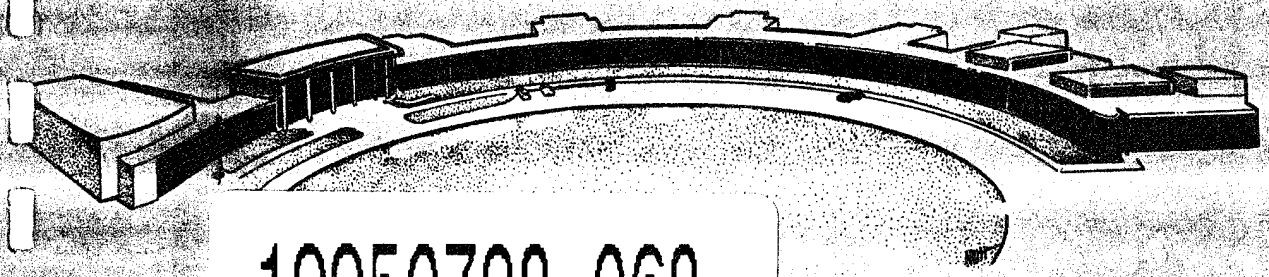

THE UNIVERSITY of TENNESSEE
SPACE INSTITUTE

Tullahoma, Tennessee

JGK

MULTIPLEXED LASER INDUCED FLUORESCENCE AND NON-EQUILIBRIUM PROCESSES IN ARCJETS

Dennis Keefer
Robert Rhodes
Trevor Moeller
David Burtner

University of Tennessee Space Institute
Center for Laser Applications
MS 24, B. H. Goethert Parkway
Tullahoma, Tennessee 37388-8897

Final Technical Report

for

Grant No.:
AFOSR-91-0200

Performance Period:
March 15, 1991 - September 14, 1994

REPORT DOCUMENTATION PAGE

Form Approved
OMB No. 0704-0188

1. AGENCY USE ONLY (Leave blank)	2. REPORT DATE	3. REPORT TYPE AND DATES COVERED
	November 14, 1994	Final Technical Report/3-15-91 - 9-14-94

4. TITLE AND SUBTITLE
Multiplexed Laser Induced Fluorescence and Non-Equilibrium Processes in Arcjets

5. FUNDING NUMBERS
$308,764.00

AFOSR-91-0200

6. AUTHOR(S)
Dennis Keefer, David Burtner, Trevor Moeller, and Robert Rhodes

7. PERFORMING ORGANIZATION NAME(S) AND ADDRESS(ES)
University of Tennessee Space Institute
Center for Laser Applications
MS 24, B. H. Goethert Parkway
Tullahoma, TN 37388-8897

8. PERFORMING ORGANIZATION REPORT NUMBER

9. SPONSORING / MONITORING AGENCY NAME(S) AND ADDRESS(ES)
AFOSR/NA Dr. Birkan
110 Duncan Avenue Suite B115
Bolling AFB, DC 20332-0001

10. SPONSORING / MONITORING AGENCY REPORT NUMBER

11. SUPPLEMENTARY NOTES

12a. DISTRIBUTION / AVAILABILITY STATEMENT
Approved for public release;
distribution unlimited.

12b. DISTRIBUTION CODE

13. ABSTRACT *(Maximum 200 words)*

For the past five years there has been an ongoing experimental and analytical program at the University of Tennessee Space Institute (UTSI) to improve our understanding of arcjet physics. A computational model that assumed local thermodynamic equilibrium was first used to simulate arcjet thrusters operating on ammonia, hydrogen, and argon. The UTSI arcjet code was later extended to include a two temperature, finite rate kinetic model for hydrogen plasma. Recently, this code has been used to simulate a radiation-cooled arcjet (MARC thruster) experiment and a water-cooled arcjet (TT1 thruster) experiment performed at The Universitat Stuttgart Institut fur Raumfahrtsysteme. The results of these simulations are presented along with a review of UTSI arcjet computation code development. A two-beam multiplexed laser induced fluorescence (LIF) technique was developed at UTSI to provide detailed measurements of arcjet flows near the nozzle exit plane. Comparison of detailed flowfield measurements with predictions of the computation model were used to provide insight into the physical models used in the arcjet code. The method was first demonstrated using a small, 300 W, water-cooled arcjet operated with argon propellant. The method was then applied to a 1 kW arcjet operated with hydrogen and nitrogen propellant mixtures using the Balmer alpha line of hydrogen. Recently, the method has been extended to use an excited state line in nitrogen. The results of this most recent research are presented.

14. SUBJECT TERMS	15. NUMBER OF PAGES
	16. PRICE CODE

17. SECURITY CLASSIFICATION OF REPORT	18. SECURITY CLASSIFICATION OF THIS PAGE	19. SECURITY CLASSIFICATION OF ABSTRACT	20. LIMITATION OF ABSTRACT
Unclassified	Unclassified	Unclassified	None

MULTIPLEXED LASER INDUCED FLUORESCENCE AND NON-EQUILIBRIUM PROCESSES IN ARCJETS

D. Keefer,* D. Burtner,** T. Moeller,† and R. Rhodes‡
University of Tennessee Space Institute
Center for Laser Applications
Tullahoma, TN 37388-8897

Abstract

For the past five years there has been an ongoing experimental and analytical program at the University of Tennessee Space Institute (UTSI) to improve our understanding of arcjet physics. A computational model that assumed local thermodynamic equilibrium was first used to simulate arcjet thrusters operating on ammonia, hydrogen, and argon. The UTSI arcjet code was later extended to include a two temperature, finite rate kinetic model for hydrogen plasma. Recently, this code has been used to simulate a radiation-cooled arcjet (MARC thruster) experiment and a water-cooled arcjet (TT1 thruster) experiment performed at The Universitat Stuttgart Institut fur Raumfahrtsysteme. The results of these simulations are presented along with a review of UTSI arcjet computation code development. A two-beam multiplexed laser induced fluorescence (LIF) technique was developed at UTSI to provide detailed measurements of arcjet flows near the nozzle exit plane. Comparison of detailed flowfield measurements with predictions of the computation model were used to provide insight into the physical models used in the arcjet code. The method was first demonstrated using a small, 300 W, water-cooled arcjet operated with argon propellant. The method was then applied to a 1 kW arcjet operated with hydrogen and nitrogen propellant mixtures using the Balmer alpha line of hydrogen. Recently, the method has been extended to use an excited state line in nitrogen. The results of this most recent research are presented.

Introduction

An effort has been underway at The University of Tennessee Space Institute (UTSI) since 1989 to develop a better understanding of arcjet physics using computational simulations and optical diagnostics. We will review the past development of our arcjet simulation code and our multiplexed laser induced fluorescence (LIF) measurements and then present the results of our most recent research.

The UTSI computational code was originally developed to simulate a laser sustained plasma thruster [1]. A steady-state, Navier-Stokes code based on the SIMPLE algorithm of Gosman and Pun [2] as modified by Rhie [3] to handle subsonic and supersonic flows was extended to include radiation transfer and heat addition [4]. The code proved successful at predicting the behavior of laser sustained plasmas [1] and radio frequency inductive arcs [5], and was therefore chosen as a basis for further development to permit arcjet simulations. The original code assumed that the plasma was at local thermodynamic equilibrium (LTE), which proved reasonable for laser sustained plasmas that typically are operated at pressures of one to several atmospheres. Later, Zerkle developed a non-equilibrium code for laser sustained plasmas [6].

Initial comparisons of the UTSI arcjet code with experiments performed at NASA Lewis Research Center [7] using a 10 kW hydrogen arcjet showed that the code overestimated performance, but predicted correct trends with propellant flow rate and power. Subsequent comparisons of the code with the experimental performance of similar water-cooled and radiation-cooled arcjets revealed the inadequacy of the LTE assumption [8]. The code has now been extended to include a two temperature, finite rate kinetic model for the plasma, and predictions with the new code are significantly improved. These new results will be described later.

The velocity distribution function of an absorbing atom can be sampled with a high degree of precision using narrow line tunable dye lasers [9]. For propellants of interest in arcjets, the only candidates for this technique are excited state atoms, since the resonance absorption lines are all in the vacuum ultraviolet portion of the spectrum. This technique was first demonstrated in an arcjet plume using the Balmer alpha transition in hydrogen [10]. We proposed and developed a multiplexed LIF method which is capable of measuring two (or more) components of velocity simultaneously. This method was first demonstrated using a 300 W arcjet operating with argon propellant [11]. Subsequently, we have used this technique to measure the exhaust plume velocity in a 1 kW arcjet using ammonia and hydrazine analog mixtures of hydrogen and nitrogen using both H-alpha and nitrogen transitions. These new results will also be presented later.

---

* B. H. Goethert Professor of Engineering Science & Mechanics, Member, AIAA

** GRA, Student Member, AIAA

† GRA, Student Member, AIAA

‡ Senior Engineer, Member, AIAA

2.0 The UTSI Arcjet Simulation Codes

The general form of the UTSI arcjet model is a Navier-Stokes solver based on the Semi-Implicit Pressure Linked Equation (SIMPLE) algorithm of Gosman and Pun [2], which was modified by Rhie to handle subsonic and supersonic flows [3]. The capabilities for heat addition and radiation heat transfer were later added by Jeng and Keefer [4]. The UTSI arcjet model has been extended to remove the assumptions of equilibrium chemical composition and LTE. The latter assumption has been replaced with a two temperature model for the electrons and the heavy gas. With a few significant exceptions, the current formulation for the non-equilibrium model was described in a paper presented at the 23rd International Electric Propulsion Conference [12]. Since that work was presented, the model has also been modified to remove the constraints of specified power dissipation and specified current distribution on the anode.

2.1 The Equilibrium Arcjet Simulation Code

Numerical modeling of the fluid dynamics in an arcjet is a complicated task. Three momentum equations, the energy equation, and the continuity equation must be solved simultaneously with three electromagnetic equations. The UTSI arcjet model takes advantage of several assumptions and simplifications to make the problem manageable.

The UTSI code [13] uses the fluid equations for steady, axially symmetric, compressible flow. In the equilibrium model, local thermodynamic and chemical equilibrium is assumed everywhere. This assumption implies that heavy particle and electron temperatures are equal and that all thermodynamic and transport properties, including species concentrations, can be defined by two state variables. The flow is assumed to be laminar. The electromagnetic equations are also steady in time and axially symmetric. The axial and radial components of the magnetic field are assumed to be zero.

One exception to the assumption of local thermodynamic equilibrium (LTE) is made to account for non-equilibrium effects of electrical conductivity. Changes to the electrical conductivity can greatly influence the character of the flow because this property controls the current distribution and the electrical power absorption in the flow. The assumption of LTE causes the conductivity to be a function of pressure and static enthalpy. However, in certain areas of the flow, such as in the downstream expansion and near the anode wall, the gas is not in equilibrium. In particular, assuming LTE in the boundary layer near the anode seriously changes the physics of the model. Under true LTE conditions, the relatively cold boundary layer would have an extremely low conductivity that would raise the voltage at the wall causing the character of the arc reattachment to be unrealistic. Under actual conditions, the boundary layer at the anode has enhanced electron concentration due to chemical and thermodynamic non-equilibrium in the boundary layer. Compensation for the non-equilibrium effects is achieved by artificially enhancing the electrical conductivity at the anode. Near the wall, the conductivity is not allowed to decrease at low temperatures as it would under an LTE calculation. Figure 1 shows this effect graphically.

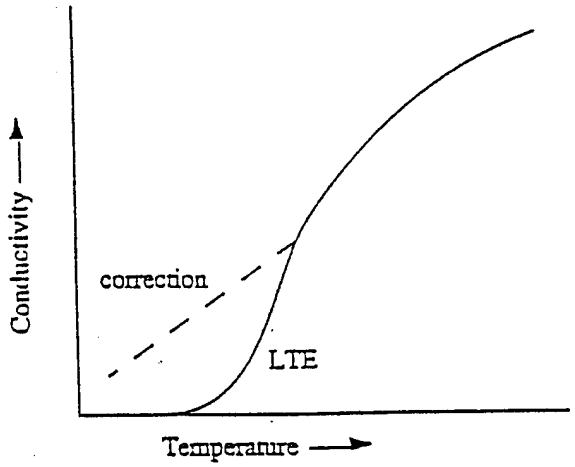

Figure 1. Electrical conductivity modification used in the LTE version of the simulation code.

2.1.1 Governing Equations

The model solves for eight dependent variables from eight coupled partial differential equations. The dependent variables are axial velocity (u), radial velocity (v), azimuthal velocity (w), static enthalpy (H), pressure (p), the azimuthal component of magnetic field (B_θ), and the axial and radial current densities (J_x) and (J_r). The electromagnetic equations are coupled to the fluid equations through Ohmic heating and Lorentz body forces. The following symbols are used in the governing equations:

x	axial coordinate
r	radial coordinate
ρ	gas density
μ	viscosity
c_p	specific heat at constant pressure
k	thermal conductivity
σ	electrical conductivity
q_i	Ohmic heating
q_r	radiation loss
Φ	viscous dissipation
$\mathbf{v}$	vector velocity

The velocity components are obtained from conservation of momentum in three directions. The mo-

mentum equation in vector notation is:

$$\nabla \cdot \rho \mathbf{v} \cdot \mathbf{v} = \nabla \cdot \mu \nabla \mathbf{v} - \nabla p - \nabla \times (\mu \nabla \times \mathbf{v}) + \mathbf{J} \times \mathbf{B} \tag{2.1}$$

The static enthalpy is obtained from the energy equation

$$\nabla \cdot \rho \mathbf{v} H = \nabla \cdot \frac{k}{c_p} \nabla H + \Phi + q_i - q_r + \mathbf{v} \cdot \nabla p \tag{2.2}$$

which includes the viscous dissipation term. For axisymmetric flow the viscous dissipation is,

$$\Phi = \mu \left[\begin{array}{l} 2 \left\{ \left(\frac{\partial v}{\partial r} \right)^2 + \left(\frac{v}{r} \right)^2 \right. \\ \qquad \left. + \left(\frac{\partial u}{\partial x} \right)^2 \right\} \\ \qquad + \left(\frac{\partial w}{\partial x} \right)^2 + \left(\frac{\partial v}{\partial x} + \frac{\partial u}{\partial r} \right)^2 \\ \qquad + \left(\frac{\partial w}{\partial r} - \frac{w}{r} \right)^2 \\ \qquad - \frac{2}{3} \left(\frac{\partial v}{\partial r} + \frac{v}{r} + \frac{\partial u}{\partial x} \right)^2 \end{array} \right] \tag{2.3}$$

The Ohmic heating term is given by,

$$q_i = \frac{\left(J_x^2 + J_r^2 \right)}{\sigma} + B_\theta \left(v J_x - u J_r \right) \quad . \tag{2.4}$$

The radiation transport in the energy equation is modeled by assuming optically thin and optically thick components as used by Jeng and Keefer [4]. The optically thick radiation is modeled using the Rosseland [14] approximation which adds a term to the local thermal conductivity of the gas. The optically thin radiation is treated as energy lost from the system. The pressure is obtained from the continuity equation.

$$\nabla \cdot \rho \mathbf{v} = 0 \tag{2.5}$$

The electromagnetic properties of the flow are described by Maxwell's equations and Ohm's law using the MHD approximation which neglects displacement current and assumes that the fluid is electrically neutral:

$$\nabla \times \mathbf{B} = \mu_0 \mathbf{J} \tag{2.6}$$

$$\nabla \times \mathbf{E} = 0 \tag{2.7}$$

$$\nabla \cdot \mathbf{B} = 0 \tag{2.8}$$

$$\nabla \cdot \mathbf{E} = 0 \tag{2.9}$$

$$\mathbf{J} = \sigma \left[\mathbf{E} + (\mathbf{v} \times \mathbf{B}) \right] \tag{2.10}$$

where μ_0 is the permeability of free space, σ is the electrical conductivity and **B**, **E**, **v**, and **J** are the vector quantities of magnetic field, electric field, velocity, and current density. These equations are combined and simplified by assuming axial symmetry and by assuming that the radial and axial components of magnetic field are zero. The resulting equation for azimuthal magnetic field written in terms of the combined variable $\beta = rB_\theta$ is,

$$\frac{\partial}{\partial x} \left(\frac{1}{\sigma} \frac{\partial \beta}{\partial x} \right) + r \frac{\partial}{\partial r} \left(\frac{1}{r\sigma} \frac{\partial \beta}{\partial r} \right) = \mu_0 \left[\frac{\partial}{\partial x} (\beta u) + r \frac{\partial}{\partial r} \left(\frac{\beta v}{r} \right) \right] \tag{2.11}$$

and the components for current density are written,

$$J_x = \frac{1}{\mu_0 r} \frac{\partial \beta}{\partial r} \tag{2.12}$$

$$J_r = \frac{-1}{\mu_0 r} \frac{\partial \beta}{\partial x} \tag{2.13}$$

The governing Eqs. 2.1 through 2.13 are solved in a transformed coordinate system, which is a mapping of the true nonorthogonal and nonuniform grid to a grid of unit squares. Nonlinear terms are linearized by including them in source terms [15]. Equation 2.11, which describes the magnetic field, is linear in β. It is solved by direct matrix inversion. A solution for β is typically calculated every 20 iterations. The solution is relaxed into the previous solution with Eq. 2.14. The fluid equations for u, v, w, H, and p are solved sequentially using updated values of the dependent variables when they are available and the old values when updated ones have not yet been calculated. As the new values of the dependent variables are calculated, they also are relaxed into the previous solution according to Eq. 2.14,

$$\phi = (1 - f_r)\phi_{\text{old}} + f_r \phi_{\text{new}} \quad . \tag{2.14}$$

In Eq. 2.14, ϕ is any dependent variable $(u, v, w, H, p,$ or $\beta)$ and f_r is a relaxation factor between zero and one. A typical value for f_r is 0.2. Solution iterations continue until the residual errors of the equations have been reduced to reasonably small values. Upwind differencing for convective terms and fourth order pressure smoothing maintain stability of the dependent variables before a final solution is determined [3].

2.1.2 Boundary Conditions

A no-slip velocity boundary condition is in effect at all walls. The wall temperatures are specified a *priori* at each axial location, and the normal pressure gradient on the walls is zero. The radial components of u and v and the derivatives of u, H, and p are set to zero along the symmetry line at the center of the flow. The axial derivatives of all dependent variables are set to zero at the nozzle exit. Velocity and enthalpy are specified at the inlet based on the mass flow, inlet temperature, and inlet swirl angle, which are input parameters to the program. The boundary condition for the magnetic field is specified with the combined variable β. The boundary condition on β is determined from the axial component of the current by integration of Eq. 2.12 with respect to r from the center of the flow to the wall at each axial location. This yields the equation

$$\beta_{\text{wall}} = (B_\theta r)_{\text{wall}} = \mu_0 \int_0^{r_{\text{wall}}} J_x r dr = \frac{\mu_0 I}{2\pi} \tag{2.15}$$

where I is the total current inside the boundary of interest at a particular axial location. Therefore, β can be specified on the cathode and anode walls if the current I is known at each axial location. The current in the arcjet originates at the cathode tip, and is assumed to flow axially and uniformly into the gas over an area of about one percent of that of the constrictor. The current flow into the nozzle wall is assumed to be linearly distributed in the expansion section of the nozzle. Current is not allowed to extend past the nozzle exit plane. These assumptions are based on observations of arcjets in operation [16]. Because a value for I can be specified for all axial locations, the magnetic field can be calculated on all boundaries.

Recently, the assumption of a linear distribution of current on the anode has been relaxed by changing the boundary condition on β from a specified value to a zero normal gradient, starting just downstream of the end of the constrictor. This has the effect of putting a constant voltage boundary condition on the nozzle and allows the current distribution to adjust depending on the plasma conductivity. This is a more realistic representation of the boundary physics, and results in a significant change in the current distribution on the anode.

A limitation is placed on the total electrical power absorbed by the flow. The model calculates local power absorption from local current and conductivity. The model assumes LTE, which results in values of electrical conductivity in the flow which may differ considerably from those in a non-equilibrium state. The conductivity dictates the power absorption which, in turn, affects the entire flow. To allow for the general uncertainty in the electrical conductivity, the sum of calculated absorbed power from each computational location in the flow is forced to equal a predetermined total power. This is accomplished by multiplying the power absorbed at each computational location by the ratio of the specified total power input to the absorbed power summed throughout the flow. This correction insures that the correct total power is deposited into the flow. The correction was first added to a precursor to the UTSI arcjet code, a code developed to simulate inductive radio frequency arc discharges, to aid in stability [5].

The constraint on total power has also been relaxed for our most recent calculations. Since power supplies usually regulate current, total power is an experimental result, and it is more realistic to allow the calculated results to predict the total power. For these new calculations, the total current is specified, and the total power is determined by the integral of q_i over the volume of the arcjet.

2.1.3 Equilibrium Thermodynamic and Transport Properties

The thermodynamic and transport properties used by the code are stored in lookup tables that the program can access during operation. Temperature is stored as a function of static enthalpy for a range of pressures. The transport properties viscosity (μ), thermal conductivity (k), and electrical conductivity (σ) are stored as functions of temperature and pressure [15].

The ammonia property tables were calculated by R. J. Zollweg [17] using collision cross section data for a hydrogen and nitrogen mixture. The calculations were made for a non-ideal plasma in local thermodynamic equilibrium. The electrons in a non-ideal plasma have kinetic energies of the order of the Coulomb potential, so that only a few electrons are inside a Debye sphere [18]. Zollweg writes that non-ideal plasmas occur "at relatively low temperatures but relatively high electron densities." These conditions can exist over a significant portion of the arcjet flowfield [18].

Local thermodynamic equilibrium (LTE) and chemical equilibrium are assumed in the hydrogen equilibrium code. Therefore, temperature and species concentrations are functions of static enthalpy and pressure only. The temperature is tabulated as a function of enthalpy for a range of pressures and is obtained by table lookup as needed. The transport properties: viscosity, thermal conductivity, and electrical conductivity, are tabulated as functions of temperature and pressure. The program used to generate these properties [19] uses tabulated collision cross section data for the H_2, H, H^+, e system and outputs the internal thermal conductivity, electrical conductivity, viscosity, and the binary diffusion coefficients. Ambipolar diffusion is assumed for the electrons since the model assumes no charge separation.

The radiation from hydrogen as a function of

temperature and pressure at chemical and thermodynamic equilibrium were calculated using the methods described by Griem [20]. Energy transport by radiation is modeled as an optically thin component which results in a direct energy loss from the system, and an optically thick component which is used to define an equivalent thermal conductivity using the Rosseland approximation [14]. An effective thermal conductivity is calculated as the sum of the internal conductivity, the conductivity from the Rosseland approximation, and the energy transport resulting from the diffusion of species [21].

2.2 The Non-equilibrium Arcjet Simulation Code

The LTE model for the plasma is replaced by a model which provides separate temperatures for the electrons and heavy particles and finite-rate chemical kinetics. The form of the momentum and continuity equations are the same for both the equilibrium and non-equilibrium models. The density used in these equations is modified to account for the two temperature plasma. Starting with the definition of the partial pressure for any species $(p_i = n_i k T_i)$, the mixture density $(\rho = \sum n_i m_i)$, and the mixture pressure $(p = \sum p_i)$, the mixture density may be written:

$$\rho = pM/R\left[T_h + (T_e - T_h)x_e\right] \quad , \qquad (2.16)$$

where M is the mixture molecular weight, R is the gas constant, and x_e is the electron mole fraction.

2.2.1 Mixture Enthalpy

In equilibrium flow, the energy transported by diffusion of species may be combined with the term containing $k\nabla T$, since the species gradients may be written in terms of the temperature gradient. For flow that is not in equilibrium, these terms must be considered separately. In this case, the equation for mixture enthalpy becomes:

$$\begin{aligned}\nabla \cdot \rho \mathbf{v} H &= \nabla \cdot [k/c_{p_h} \nabla H \\ &+ (\rho D - k/c_{p_h}) \sum h_i \nabla \alpha_i - k \alpha_e c_{p_e}/c_{p_h} \nabla T_e] \\ &+ \Phi + q_i - q_r + \mathbf{v} \cdot \nabla p \qquad (2.17)\end{aligned}$$

where c_{p_h} is the sum of $c_{p_i}\alpha_i$ over the heavy species, and subscript e represents electrons.

2.2.2 Electron Energy

The assumption of LTE made in our previous work is relaxed in the non-equilibrium model by assuming the electron gas and the heavy particles have separate temperatures, both with a Maxwell-Boltzmann distribution. This requires a separate energy equation for the electron gas. In this equation the electrical Ohmic heating is balanced by electron convection, conduction, diffusion, and energy transfer to the heavy particles by collisions. The form of the equation and the included terms are taken from Park [22],

$$\begin{aligned}\nabla \cdot \rho \mathbf{v} \alpha_e h_e - \nabla \cdot [k_e \nabla T_e + h_e D \nabla \alpha_e] \\ - \mathbf{v} \cdot \nabla p_e = S \qquad (2.18)\end{aligned}$$

where $S = q_{ce} + q_{ch} + q_i - q_r$.

The term describing the work done by the electron-pressure gradients $(\mathbf{v} \cdot \nabla p_e)$ is obtained using the assumption that the electrons and heavy species share the same flow velocity. The electron partial pressure is,

$$p_e = p T_e x_e / [T_h + (T_e - T_h) x_e] \qquad (2.19)$$

where x_e is the mole fraction of electrons.

The term q_{ce} represents the energy transfer between the heavy gas and the electron gas resulting from collisions of electrons with the heavy species,

$$q_{ce} = \sum 2 n_e \frac{m_e}{m_i} \nu_i \frac{3}{2} k (T - T_e) \quad . \qquad (2.20)$$

The collision frequency (ν_i) is evaluated from the temperature dependent collision cross-sections for electron-heavy collisions evaluated at the electron temperature using the transport properties program described in Section 2.2.5.

The term q_{ch} represents the energy transport to the electron gas resulting from the participation of electrons in chemical reactions. It is assumed that in reactions where an electron is the third body the dissociation or ionization energy comes from the electron gas, lowering the electron temperature, and the energy of recombination goes to the electron gas, raising the electron temperature.

The energy input to the system (q_i) and the radiation from the system (q_r) are evaluated in the same way as they are in the equilibrium model.

2.2.3 Species

Three species equations were added to the system of equations to allow the calculation of flows where dissociation of H_2 and ionization of H are not in equilibrium. The mixture is assumed to consist of four species: molecular hydrogen (H_2), atomic hydrogen (H), ionized hydrogen (H^+), and electrons (e). With the assumption of electrical neutrality, the electron and ion concentrations are equal, and one

species equation can be eliminated. The equation for conservation of a species may be written as,

$$\nabla \cdot \rho v \alpha = \nabla \cdot \rho D \nabla \alpha + S_\alpha \quad , \qquad (2.21)$$

where S_α is the production of the species by chemical reaction. A residence time is evaluated from the mass in a computational cell divided by flux into the cell, and the species production equations are solved over this residence time step using a linearized set of equations for the four species [23]. The source term then becomes the change in the species concentration divided by the time for the step.

2.2.4 Boundary Conditions

Additional boundary conditions are required for the electron temperature and the species equations for the nonequilibrium flow model. The walls are assumed to be catalytic for electron-ion and H atom recombination, have a no-slip boundary condition and a specified temperature distribution. As a consequence, the gas is in equilibrium at the wall temperature. Transport properties at the wall are evaluated at the conditions of the first computational point inside the wall. The gas is assumed to be in equilibrium at the inlet, although a minimum mole fraction of 10^{-10} is set for any species throughout the flowfield. The two temperatures are constrained to a minimum value of 100 K.

2.2.5 Transport Properties for Non-equilibrium Hydrogen

Transport properties in a two temperature model with non-equilibrium species concentrations depend on the two temperatures and the number densities of all the species. For non-equilibrium hydrogen the properties are a function of five variables representing the two temperatures, the total number density, and the degree of dissociation and ionization. Both a five dimensional table lookup and direct calculation at each field point are impractical, so we decided to combine curve fitting, table lookup, and some simplifying assumptions to give a procedure that is both accurate and reasonably fast. One requirement is that the properties vary smoothly over a wide range of variables to avoid instabilities while the solution is converging.

The program we are using to obtain the transport properties [19] uses theoretical and experimental collision cross-section data to obtain collision integrals from which the transport properties are calculated. It was found that the transport properties at constant pressure and species mole fraction could be fitted to an equation of the form $z = aT^n$ where T is the electron temperature for electron thermal conductivity (k_e) and electrical conductivity (σ), and T is the heavy gas temperature for heavy gas thermal conductivity (k_h), and viscosity (μ).

The thermal conductivity of the electron gas used in the electron energy equation is taken to be k_e. Park [22] shows that this value may be too high, since part of the energy transfer implicit in this coefficient is transferred to the heavy particles.

For k_e and σ the coefficients a and n are functions of pressure and electron concentration, but were found to be relatively insensitive to the degree of dissociation of H_2. Therefore, the H_2/H ratio is not accounted for in the fit coefficients. The properties k_h and μ are calculated for each species and are combined for the mixture. For the electron-ion pair the fit coefficients were found to be functions of pressure, while for H_2 and H they are constants. The best way found to get the mixture properties is to sum the product of the mole fraction and the species property. For the present case, this procedure gave results much closer to those calculated for the actual mixture than did the Wilke mixture rule [24].

The procedure described above was checked by comparing its results with those for equilibrium mixtures using the transport property program. The agreement is within a few percent for all the cases checked.

The binary diffusion coefficients $(\mathcal{D}_{ij})$ are equal to cT^2/p where c is a function of p for $\mathcal{D}_{H,H_2}$ and a constant for $\mathcal{D}_{H,H^+}$ and $\mathcal{D}_{H_2,H^+}$. The coefficients involving ions are mutiplied by $(1 + T_e/T_h)$ to account for ambipolar diffusion. In these flows there are few locations where H_2 and the electron-ion pair coexist. A single diffusion coefficient for the mixture was used, rather than the much more complicated, but correct, method of calculating multicomponent diffusivities. To provide a smooth transition across regions where all three components coexist, a heurestic mixture rule is used,

$$D = (\alpha_1\alpha_2\mathcal{D}_{12} + \alpha_1\alpha_3\mathcal{D}_{13} + \alpha_2\alpha_3\mathcal{D}_{23}/ \\ (\alpha_1\alpha_2 + \alpha_1\alpha_3 + \alpha_2\alpha_3) \quad . \qquad (2.22)$$

This gives the correct answer for a mixture of any two components and provides a smooth transition where three component mixtures exist.

3.0 Multiplexed Laser Induced Fluorescence Velocimetry

A two-beam multiplexed laser induced fluorescence (LIF) technique was developed to provide detailed measurements of arcjet flows near the nozzle exit plane. Comparison of detailed flowfield measurements with predictions of the computational model were used to provide insight into the physical models used in the code [25]. The method was first demonstrated using a small, 300 W, water-cooled arcjet operated with argon propellant [11]. The method was then applied to a 1 kW arcjet operated with hydrogen

Balmer alpha line of hydrogen. Recently, the method has been extended to use an excited state line in nitrogen [26].

The Doppler principle for measuring flow velocities with LIF has been known for some time. Zimmerman and Miles [27] reported an LIF technique to measure the velocity in a hypersonic wind tunnel in 1980. A narrow line, tunable dye laser is used to excite an atom in the flow. Fluorescence from the excited atom is detected as the laser is tuned across the absorption line profile. The wavelength at which the line is excited depends, through the Doppler effect, on the velocity of the atom. If the spectral width of the laser is small compared to the absorption Doppler profile of the atom, then the measured line profile is a measure of the velocity distribution function of the atoms. Thus, in principle, mean velocity along the laser beam direction and temperature can be determined from the measured Doppler line profile.

In the multiplexed LIF technique the laser beam is divided into two beams which are recombined with an angle between them. Each beam is modulated at a different frequency and phase-lock detection is used to separate the fluorescence induced from each beam. The velocity along each of the beam directions can be combined to provide a simultaneous vector measure of velocity. One difficulty with this technique is that an accurate, unshifted reference wavelength must be measured to obtain an accurate absolute velocity. We solved this problem by using an optogalvanic cell to provide a continuous, simultaneous reference using the same atomic transition [28]. A schematic of a typical experimental arrangement is shown in Fig. 2.

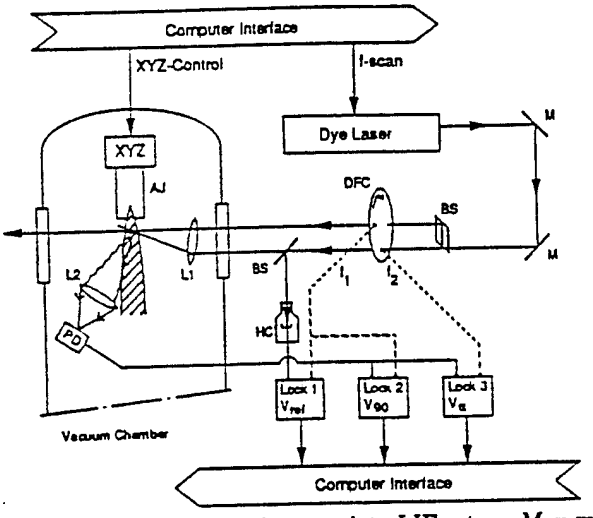

Figure 2. Schematic of the complete LIF setup: M = mirror, BS = beam splitter, DFC = dual frequency chopper, HC = hollow cathode lamp, L1 = focusing lens, L2 = collection lens, PD = photodiode (with pinhole aperture), AJ = arcjet, and LOCK = phase-locked amplifier.

3.1.1 Description of the Multiplexed LIF Technique

A detailed theoretical analysis of the multiplexed LIF technique is given by Ruyten and Keefer [11]. Here we will present only the elements essential to understanding the basic process.

It is assumed that the velocity distribution of the diagnostic species in the arcjet plume is described by $f(v_x, v_y)$, where v_x and v_y are the velocity components parallel and perpendicular to the arcjet axis. The mean velocity components $< v_x >$ and $< v_y >$ are given by the first moments of the distribution function,

$$< v_{x,y} >= \int_{-\infty}^{\infty}\int_{-\infty}^{\infty} v_{x,y} f(v_x, v_y) dv_x dv_y \quad (3.1)$$

The Doppler shift in velocity, v_D is given by,

$$v_D = -\lambda(\nu_L - \nu_0) \quad (3.2)$$

where λ is the wavelength of the transition, ν_L is the laser frequency and ν_0 is the center frequency of the unshifted atomic transition. If the homogeneous linewidth of the absorption process (laser linewidth and homogeneous atomic linewidth) is small compared to the Doppler linewidth, then the LIF signal produced by the beam at angle ϕ to the centerline is given by,

$$S_\phi(v_D) = C_\phi \int\int_{\text{band}} f(v_x, v_y) dv_x dv_y \quad (3.3)$$

where C_ϕ is an experiment-dependent constant. The "band" of integration is given by the Doppler resonance condition,

$$|v_x \cos\phi + v_y \sin\phi - v_D| < \frac{1}{2}\Delta\nu \quad (3.4)$$

where $\Delta\nu$ is the small homogeneous linewidth of the excitation process. Since the homogeneous linewidth is much smaller than the Doppler width, the signal is essentially proportional to the component of the velocity distribution function in the direction ϕ. Thus, it is possible using Eq. 3.1 to determine the mean velocity $< v_\phi >$ in the directions ϕ for both beams.

In practice, one beam is directed perpendicular to the arcjet axis and the second beam is directed along an angle ϕ chosen to provide a Doppler shift within the scan range of the tunable laser, Fig. 3.

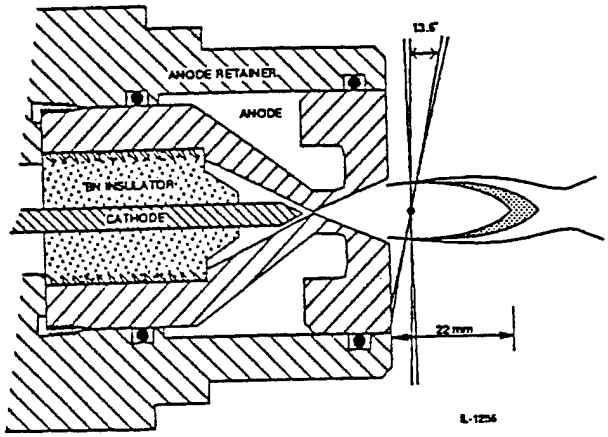

Figure 3. Schematic of the arcjet and the two diagnostic laser beams. The dot at the intersection of the laser beams represents the detection volume, as defined by the detection optics.

Since the distribution function in arcjet flows is essentially Maxwellian, the Doppler line profile is Gaussian. The radial component of the mean velocity, $< v_y >$, is determined directly from the perpendicular beam. For Gaussian line profiles the velocity is determined from the shift of the measured line center relative to the reference line from the optogalvanic cell using Eq. 3.2. The axial component, $< v_x >$, is then determined from the mean velocity measured along direction ϕ,

$$< v_x >= (< v_\phi > - < v_y > \sin\phi)/\cos\phi \quad . \tag{3.5}$$

In this way both radial and axial components of the mean velocity can be measured simultaneously.

Since the LIF technique measures the velocity distribution function, it is also possible, in principle, to determine the temperature of the flow from the second moments of the measured Doppler line profile. In practice, we found considerable differences in the temperatures determined in this way from the Doppler profiles obtained at different angles, resulting in a higher temperature in the direction parallel to the arcjet axis. Since the second moment is a measure of the spread in velocity, it will include fluctuations of the mean velocity, in addition to the spread in thermal velocity, when averaged over time, as required by the phase-lock instrumentation. Fluctuations in the mean velocity can occur as a result of unsteady operation of the arcjet or from turbulence in the flow. Thus, temperature measurements obtained from the Doppler profiles represent an upper limit for the true temperature in the flow.

4.0 Comparison of Code Predictions With Experiments

Predictions of the UTSI arcjet simulation code have been compared with experimental results for several different arcjets. A brief overview of these results will be given here; a more complete description can be found in the cited references.

4.1 Comparisons of Code Predictions with Experiments

The UTSI equilibrium arcjet model, which assumes local thermodynamic equilibrium (LTE), was first used to simulate a 30 kW ammonia arcjet that was tested by the Jet Propulsion Laboratory (JPL) [13]. The numerical model overestimated specific impulse (Isp) by about 12 percent, and the numerical anode to cathode voltage drop was about 20 percent high. A major conclusion of this study was that improved procedures for calculating transport properties were necessary to improve the accuracy of the model.

Next, a second version of the UTSI equilibrium arcjet model was developed for hydrogen propellant. The hydrogen and ammonia versions of the arcjet model were then used to compare the performance of a hydrogen and an ammonia arcjet of the same configuration and at the same electrical power [21]. The 30 kW arcjet configuration tested at JPL and modeled previously was chosen for this work. Several improvements had been made to the code since the first simulation. The predicted Isp was 5.6 percent lower than the earlier calculation, but was still 11 percent higher than the arcjet data. As expected, when the arcjet configuration was modeled with hydrogen propellant, the predicted Isp was 50 percent higher than the Isp for ammonia [21]. The effects of transport properties on arcjet performance were also investigated in this work. Numerical studies were made to assess the effect of transport properties on the predicted performance of the hydrogen arcjet. These studies indicated that diffusive transport is very significant even in the supersonic part of the flow, and that relatively small changes in transport properties can have a significant effect on performance. This work also showed that non-equilibrium recombination chemistry can have a large effect on transport properties. It was concluded that finite rate chemistry calculations are necessary if accurate arcjet performance is to be calculated.

Next, the UTSI equilibrium arcjet model was tested for three different nozzle configurations of a high power hydrogen arcjet at a number of power levels and mass flow rates [15]. The three nozzle configurations differed in constrictor length, constrictor diameter, nozzle half-angle and nozzle expansion ratio. Experimental data for these configurations were provided by NASA Lewis Research Center. The general trends of the data were predicted by the model.

However, both Isp and efficiency were overpredicted by the model, the Isp by as much as 10 percent and the efficiency by as much as 25 percent. The good qualitative agreement between the model calculations and the data indicated that the general procedures used in the model properly accounted for the essential physics of the flow and heat addition. The lack of quantitative agreement indicated that the numerical values used for transport properties may have been in error, and that one or more loss mechanisms were being neglected or underestimated. These results supported the need to include both a finite rate chemistry model to account for frozen flow losses, and a two-temperature model for electrons and the heavy gas.

After multiplexed LIF data on a small water-cooled argon arcjet was collected [11], detailed exit plane profiles of axial velocity, radial velocity, and temperature were available for comparison with the arcjet model. An argon version of the UTSI equilibrium arcjet model was developed for this work [25]. The model predicted axial velocities consistently higher than those determined experimentally, although the calculated and experimental velocity profiles did have a similar shape. The calculated radial velocity matched the experiment results very well. The model exit temperatures were twice those calculated from the experiment data. The differences between the experiment and the model results were believed to be the result of underprediction of the energy losses by the UTSI arcjet model. Energy losses from radiation and wall conduction in a small water cooled arcjet should be a significant fraction of the input power. The numerical solution showed essentially no energy loss. Radiative transport was not included in the model because the operating pressure was expected to be too low for the radiation of argon to be significant. It was concluded that radiation energy transfer, a two-temperature model for electrons and the heavy gas, and finite rate chemistry would be necessary to better predict experimental data.

Next, the hydrogen equilibrium code was used to simulate some interesting arcjet experiments performed at The Universitat Stuttgart Institut fur Raumfahrt Systeme (IRS) [8]. The experiments utilized two arcjets: one with a high temperature radiation-cooled anode, and a similar arcjet which used a water cooled anode. Some difficulty was experienced in convergence of the water-cooled solution. Many attempts were made to improve convergence with relatively little success. The best solution for the water-cooled arcjet was used for comparisons with the solution for the radiation-cooled arcjet. The IRS experiments showed that the efficiency of the radiation-cooled arcjet was 41.4 percent but the efficiency of the water-cooled arcjet was only 18.5 percent [8]. Our simulations of this experiment clearly revealed the inadequacies of the equilibrium model and the heuristic modification of the electrical conductivity. The efficiency prediction for the radiation-cooled arcjet was 45.1 percent, in reasonable agreement with the experiment, but the prediction for the water-cooled arcjet was 32 percent, nearly a factor two higher than the experiment [8].

Recently, the UTSI equilibrium code was used to simulate a 1 kW, ammonia arcjet whose performance was measured at NASA Lewis Research Center [26]. Thrust experiments were performed to determine specific impulse for a range of electrical power inputs and propellant flows. Computer simulations predicted specific impulse for the same arcjet geometry using identical power inputs and propellant flows. Figure 4 compares the specific impulse of the model with the experimental measurements as a function of specific energy. Specific energy is the electrical energy deposited in the flow per unit mass of propellant.

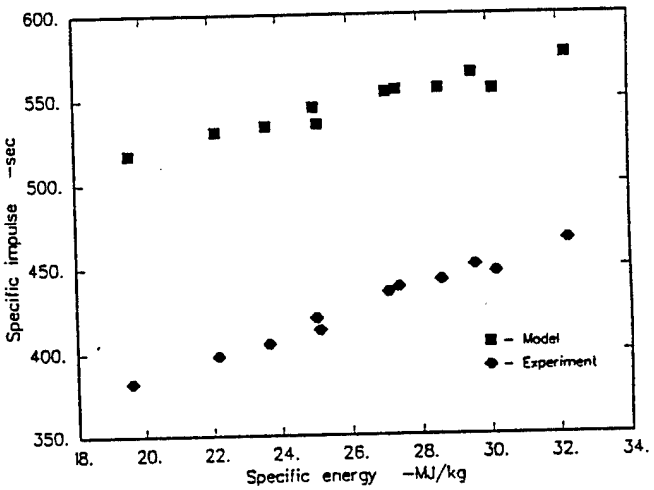

Figure 4. Comparison of measured and predicted specific impulse as a function of specific energy for a 1 kW ammonia arcjet.

Both the calculated and the measured specific impulse appear to increase linearly with specific energy. However, the predicted values significantly exceed the experimental values. This leads to the conclusion that significant energy losses have been neglected. The assumption of thermal and chemical equilibrium neglects important loss mechanisms. Non-equilibrium effects in the nozzle prevent thermal energy that has been expended in dissociation and ionization from being converted into kinetic energy during expansion. The true flow becomes frozen in a particular chemical state, but the equilibrium model allows the energy to be recovered. The equilibrium model also does not account for heat conduction to the wall by diffusion of high energy electrons from the high temperature core through the cold boundary layer. The assumption of equilibrium also alters the character of the flow by changing the electrical conductivity, which controls the distribution of power absorption.

Each time a solution from the UTSI equilibrium code was compared to experimental data, it was concluded that the equilibrium assumption should be relaxed. A new non-equilibrium version of the hydrogen arcjet code was developed which included finite rate chemistry and separate energy equations for electrons and heavy particles. Predictions from the new non-equilibrium code were compared with a high powered arcjet experiment run at NASA Lewis Research Center [12]. Some difficulty was experienced with the convergence of this solution, but the predictions of specific impulse and efficiency were in reasonable agreement with the experimental thrust and efficiency. The new non-equilibrium results underpredicted the experimental results by as much as the equilibrium code overpredicted them.

5.0 Multiplexed LIF Experiments

The multiplexed LIF technique was first used at UTSI to probe the plume of a 300 Watt argon arcjet [11]. The purpose was to demonstrate the method of using two multiplexed laser beams to measure two velocity components simultaneously and to demonstrate the method of using the optogalvanic effect in a hollow cathode discharge as a stationary reference. Argon propellant was used while proving the concept because of the large population of metastable excited states available, but the LIF technique was later applied to more applicable propellant species. LIF measurements of axial velocity, radial velocity, and temperature were obtained. A radial scan was made across the nozzle exit one millimeter downstream from the exit plane. An axial scan was obtained downstream of the nozzle along the arcjet centerline. The data indicated a radial boundary layer and a normal shock downstream from the nozzle. The location of these effects was consistent with the barrel shock and Mach disk visually observed in the plume.

Once two-beam multiplexed LIF measurements had been fully demonstrated, the technique was modified to probe the plume of a one kilowatt arcjet using simulated ammonia propellant. In preparation for the LIF measurements, several experiments were performed on the plume of the ammonia arcjet using emission spectroscopy [29]. The temperature of the plume at the exit plane was determined with three independent methods: 1) Doppler width of the hydrogen Balmer alpha line, 2) intensity ratios of the hydrogen Balmer alpha and beta lines, and 3) rotational line intensities of the NH radical. The three temperature measurements were in fairly close agreement, but the spatial trends did not agree. Emission spectroscopy was also used to make measurements of the axial velocity of the plume by observing the Doppler shift of the hydrogen Balmer alpha line. Rapid acceleration of the plume was observed downstream of the exit plane, indicating an underexpanded flow. The emission velocity data is somewhat difficult to interpret because emission spectroscopy is a line-of-sight measurement, but it is believed that emission experiments can be used to make an estimation of axial plume velocity when LIF is either impractical or not available.

The emission results were later compared to LIF measurements performed at identical conditions [30]. The LIF experiments were performed by exciting the hydrogen Balmer alpha transition. The LIF measurements confirmed the acceleration of propellant downstream of the nozzle exit as observed in emission. Several experimental factors reduced the quality of the hydrogen LIF data below that obtained with argon. The width of the hydrogen Doppler profile is similar to the maximum scan width of the laser (30 GHz) which makes the profile difficult to curve fit. In addition, the signal-to-noise ratio was high because: 1) the LIF signal obtained from the Balmer alpha transition was much less than the signal acquired from the argon transition, and 2) there was a large amount of background laser scatter.

Additional LIF measurements in the ammonia arcjet plume were made to obtain data for comparison with the UTSI arcjet simulation code [26]. The signal-to-noise ratio was greatly improved by using more sensitive optical detection and by reducing laser scatter. The LIF technique was used to measure the plume velocities and temperatures in radial scans across the exit plane. In these experiments, both the hydrogen Balmer alpha line and a transition of atomic nitrogen were used in the multiplexed LIF measurements. The nitrogen profiles are much narrower than the scan width of the laser, and there were no problems fitting the data. In addition, the fluorescence could be detected at a different wavelength than the laser, virtually eliminating the effects of scattered laser radiation. The comparisons between the equilibrium model and the data are shown in Figs. 5-7.

An interesting result of these experiments was that atomic hydrogen and atomic nitrogen in the flow had different velocities (Figs. 5 and 6).

The hydrogen is expanding radially much faster than the nitrogen, but the nitrogen appears to have a slightly larger axial component of velocity. It is believed that the hydrogen is diffusing outward more rapidly because it is lighter than nitrogen.

In general, the temperatures measured with LIF are less accurate than the velocity measurements. It is more difficult for the fitting program to determine accurate widths than accurate profile centers from the experimental data. The width of the profile obtained from the fitting program is sensitive to changes in amplitude and baseline offset of the LIF signal, while the determination of the center of the profile is relatively insensitive to these effects. Useful temperature data was not obtained from atomic hydrogen because of the extreme width of the profile. A radial scan of temperatures determined using the atomic nitrogen data is shown in Fig. 7.

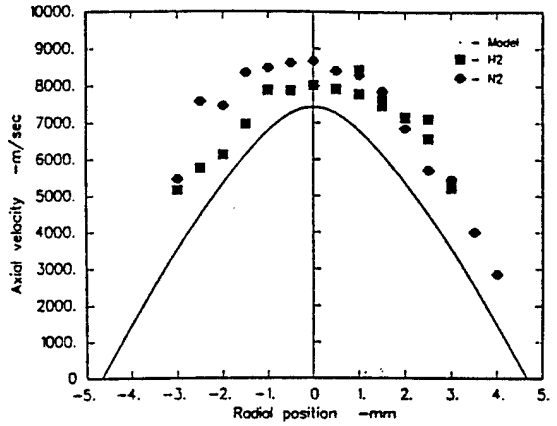

Figure 5. Measured axial velocities in the ammonia arcjet plume one millimeter from the nozzle exit. LIF measurements are shown for both atomic hydrogen and atomic nitrogen.

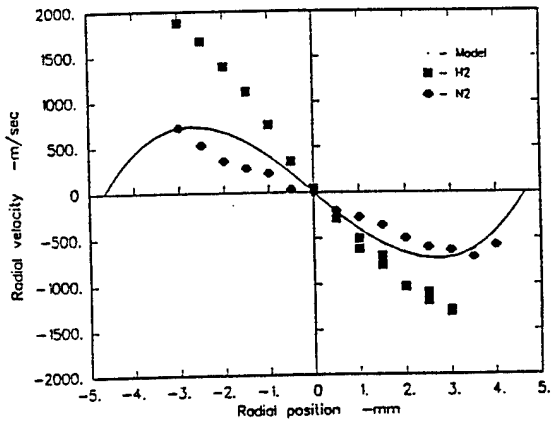

Figure 6. Measured radial velocities in the ammonia arcjet plume one millimeter from the nozzle exit. LIF measurements are shown for both atomic hydrogen and atomic nitrogen.

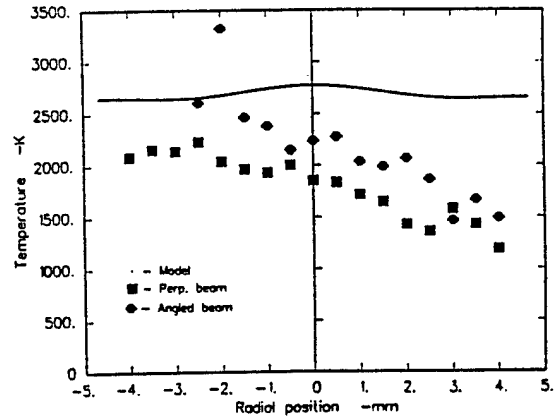

Figure 7. Measured temperatures obtained from the nitrogen LIF experiments one millimeter from the nozzle exit. Data are shown for both the perpendicular and the angled beams.

The temperatures acquired from the angled beam are consistently higher than the temperatures acquired from the perpendicular beam. This effect is believed to be caused by broadening of the Doppler profile due to spatial velocity gradients in the fluorescence collection volume. Previous experiments performed on this nozzle indicate that the propellant undergoes rapid axial acceleration after it leaves the nozzle. The velocity gradients should be larger in the axial direction than in the radial direction. Therefore, the angled beam will sample a larger variation in velocity than the perpendicular beam, and the Doppler profile detected by the angled beam will be broadened more than the profile of the perpendicular beam.

6.0 Recent Calculations Using the Non-equilibrium Code

Several significant changes have been made to the non-equilibrium code. In the present version of the code, only the value of total current is fixed, and the total power input is calculated by the code. This is now possible because the distribution of electrical conductivity within the flow calculated for the non-equilibrium plasma is more accurate than that for the LTE case. The assumption that the current flowing into the anode decreased linearly with axial position has also been dropped. Now, the current is only forced to flow into the anode in a normal direction, consistent with a constant anode potential, and the distribution of current into the anode is calculated by the code. These changes result in a more realistic simulation and have also improved convergence, although the number of iterations required to reach convergence has increased.

Calculations were made using the new version of the non-equilibrium code to compare with two arcjet experiments reported by Glocker and Auweter-Kurtz at the Institut fur Raumfahrt Systeme in Stuttgart. These are the radiation-cooled MARC thruster [31] and the water-cooled TT1 thruster [32]. Moeller has compared the UTSI equilibrium arcjet model with these experiments [8]. These experiments were selected for comparison because they have similar configurations and operating parameters, but exhibit a large difference in performance. Also, Miller and Martinez-Sanchez have used these experiments for comparison with their arcjet calculations [33]. The geometries of these thrusters are given in Table 1, and the computational grid used for both thrusters is shown in Fig. 8. Convergence is a necessary, but not sufficient, requirement for a satisfactory simulation. Various tests have been made to evaluate the quality of the solution. Several well-converged solutions have been obtained with the non-equilibrium arcjet model. Some examples of these tests are shown for a well-converged solution for the MARC thruster using the "fast" set of kinetic rates, to be described later.

Table 1. Geometric parameters for the MARC and TT1 hydrogen arcjet thrusters.

	MARC Thruster	TT1 Thruster
Constrictor Length (mm)	5.0	5.0
Constrictor Diameter (mm)	2.5	2.5
Cathode Tip Half Angle (deg)	30	30
Nozzle Area Ratio	100.	100.
Anode/Cathode Gap (mm)	2.	2.
Nozzle Half Angle (deg)	17.5	Contoured

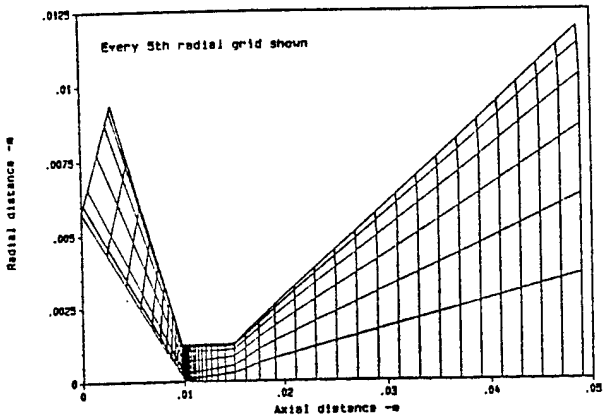

Figure 8. Computational grid used for both the MARC and TT1 hydrogen arcjet thrusters.

One test of the solution is to determine how well mass is being conserved. The radial integral of mass flow from the converged solution is shown in Fig. 9 as a function of axial location. The mass flow is typically constant to within a few percent.

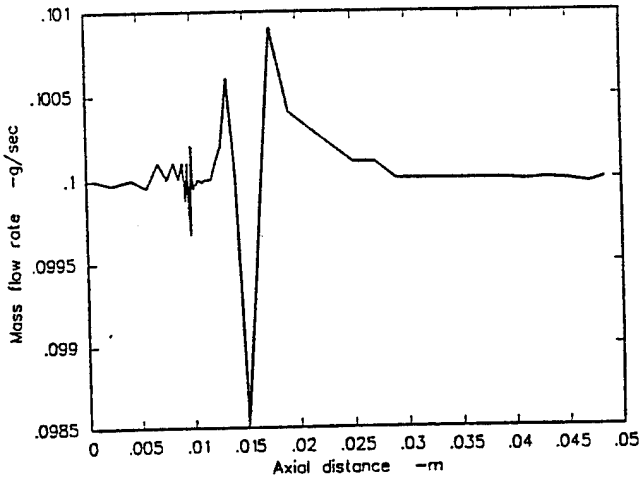

Figure 9. Radial integral of the calculated mass flow as a function of axial position for a well-converged solution. The correct mass flow is 0.1 g/s.

Power balances are checked by comparing the total energy flux in the flow (enthalpy plus kinetic energy) with the cumulative electrical power input and the cumulative wall losses. These quantities are shown in Fig. 10 together with the integrated error. The error shown in this figure is the sum of the residual errors at each grid point upstream of the axial position. The residual errors are clearly small compared with the energy input.

The quality of the solution for the electromagnetic field is evaluated by examining voltage and current distributions. The current distributions are shown in Fig. 11.

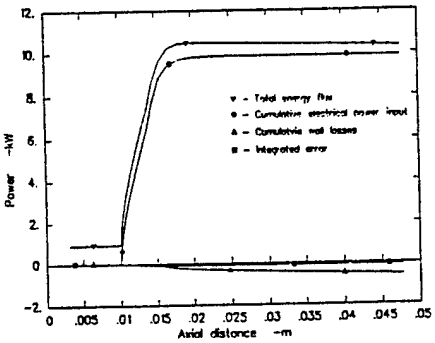

Figure 10. Comparison of the energy flux in the flow with electrical power input, wall power loss, and the residual error.

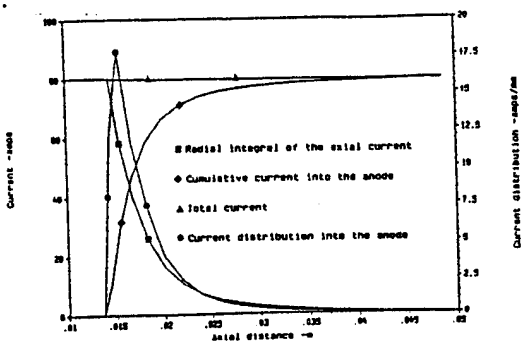

Figure 11. Current distributions. The radial integral of the axial component of current and the cumulative current into the anode sum to the specified 80 A total. Also shown is the current distribution in the anode.

The sum of the radial integral of the axial component of the current and the cumulative current flowing into the anode is essentially constant at the prescribed value of 80 amps. The current distribution into the anode is strongly peaked near the constrictor exit, but some anode current extends over the length of the nozzle.

For the steady-state case considered, $\nabla \times \mathbf{E}$ must equal zero (Eq. 2.7). This means that the line integral of electric field around any closed path must vanish. However, the calculated cathode to anode voltage is not completely independent of the path along which the voltage is calculated. How well this requirement is preserved by the code can be evaluated by comparing the voltage between the anode and the centerline as calculated along two different paths. One path begins at a point on the anode, then goes one cell toward the inlet and then radially inward to the axis. The other path goes from the point on the anode radially to the axis and then one cell toward the inlet. The results are shown in Fig. 12.

There is good agreement for the two paths except near the constrictor/nozzle corner at an axial location of 0.0155 m. The cathode-to-anode voltage, like the total electrical power input, is calculated by the code. This voltage calculated from a line integral from the cathode tip along the centerline to the axial position of the constrictor/nozzle corner, then radially to the anode and then along the anode is somewhat different than if the calculation path is along the centerline and then radially to the anode. This effect is shown in Fig. 13.

In both cases the calculated anode voltage is essentially constant along the nozzle, and the current enters the anode normal to the wall.

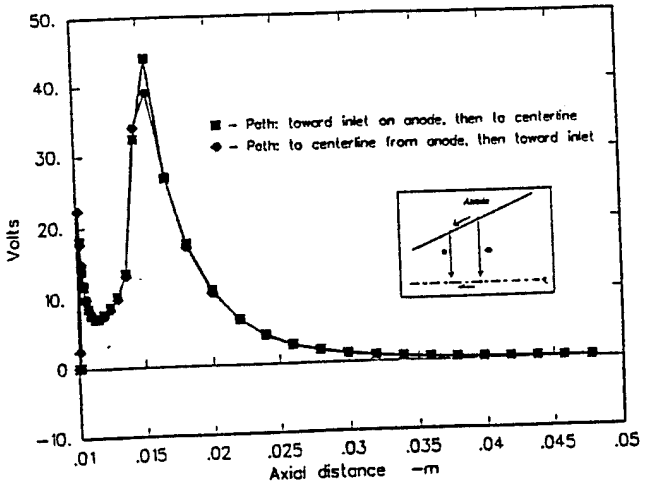

Figure 12. Anode to axis voltage calculated from the line integral along different paths.

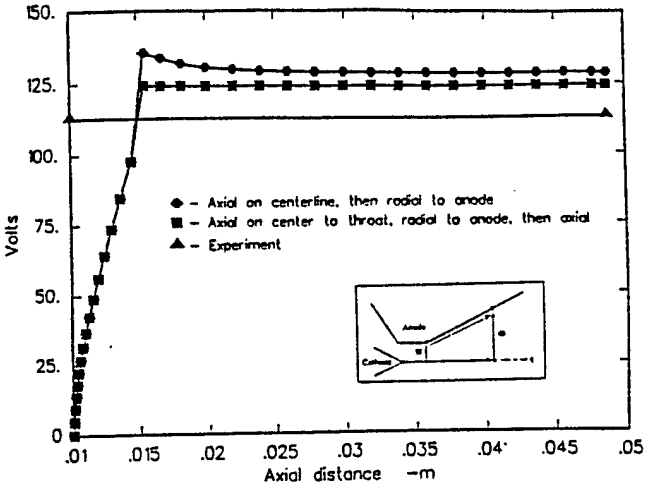

Figure 13. Voltage from the cathode tip to a point on the anode surface as calculated along two different paths. The experimental cathode-to-anode voltage of 112 V is shown for comparison.

6.1 MARC Thruster Simulations

Two calculations were made for the MARC thruster using different rates for the ionization of H atoms by electrons (Table 2). The "slow" rate used in the model was presented at the 23rd IEPC [12] with the recombination rate slightly modified to fit the data from Park [22]. The "fast" rate used the reverse rate of the recombination reaction obtained through the equlibrium constant evaluated at the electron temperature. The recombination reaction rate was taken from McCay [34] as were the rates for the other reactions in both sets.

The calculated performance for the "fast" and "slow" rates and for an equlibrium calculation are compared with the experimental data in Table 3.

The calculation with the fast chemical rates most closely matched the data. The thrust is about 6.5 percent low and the calculated power and voltage about 9 percent high. The equilibrium calculation overpredicts thrust by more than 25 percent and power by more than 50 percent. The agreement between the power calculated from the product of current and voltage and that calculated from the volume integral of J^2/σ is also better for the case run with the "fast" chemistry.

The "slow" chemistry calculation gives about 4 percent less thrust and dissipates about 8 percent more power than the "fast" chemistry case. This relatively small difference is somewhat suprising considering the large differences in predicted electron concentration shown in Fig. 14.

Table 2. Fast and slow reaction rates [12 and 34].

Forward rate $= AT^{-n}\exp(E/T)$

	Reaction	A	n	E
1	$H+H+M=H_2+M$	$6.40e+17$	1.0	0.
2	$H^+ + e + M = H + M$	$5.26e+26$	2.5	0.
3	$H_2 + e \rightarrow H + H + e$	$1.91e+11$	-1.0	$-203.$
4	$H^+ + e \rightarrow H + h\nu$	$3.77e+13$	0.58	0.
	fast rates			
5	$H^+ + e + e = H + e$	$7.08e+39$	4.5	0.
	slow rates			
5r	$H^+ + e + e \rightarrow H + e$	$2.19e+41$	5.06	0.
5i	$H + e \rightarrow H^+ + e + e$	$1.81e+14$	0.0	$-244750.$

M any third body
$\rightarrow$ one way reaction - no reverse rate
$=$ reversible reaction
- reverse rate obtained from equilibrium constant
5r recombination
5i ionization

Reaction 1 and 2, t = gas temperature
Reaction 3, 4, and 5, T = electron temperature

Table 3. Comparison of calculated results from the non-equilibrium code using two different sets of reaction rates with an equilibrium calculation and experimental data for the MARC thruster.

	Calculation			Data
	Fast Rate	Slow Rate	Equilibrium	
Area (m^2)	$.673 \times 10^{-4}$	$.673 \times 10^{-4}$	$.673 \times 10^{-4}$	$.673 \times 10^{-4}$
Mass (kg)	$.100 \times 10^{-3}$	$.100 \times 10^{-3}$	$.100 \times 10^{-3}$	$.100 \times 10^{-3}$
P_{inlet} (Atm.)	1.01	1.00	1.08	–
Thrust (N)	0.828	0.795	1.103	0.866
isp (sec)	845.3	811.3	1125.7	882.8
ke (W)	3431.	3161.	6086.	–
Efficiency	0.362	0.333	0.642	0.414
I (A)	80.2	80.2	80.2	80.2
E (V)	125.	140.	170.	112.9
EI (kW)	10.0	11.2	13.6	9.053
J^2/σ (kW)	9.863	10.68	14.10	–

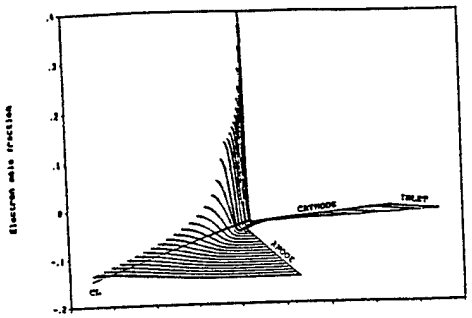

(a)

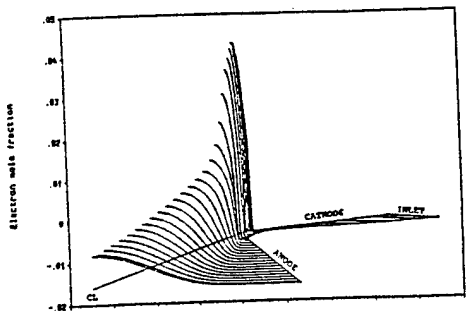

(b)

Figure 14. Calculated electron concentrations. The "fast" chemistry results are shown in (a) and the "slow" chemistry results are shown in (b).

However, the electron temperature increases when the electron concentration decreases, as shown in Fig. 15.

The result of the inverse relation between electron concentration and electron temperature is a smaller change in electrical conductivity than would occur if only the electron concentration or temperature changed.

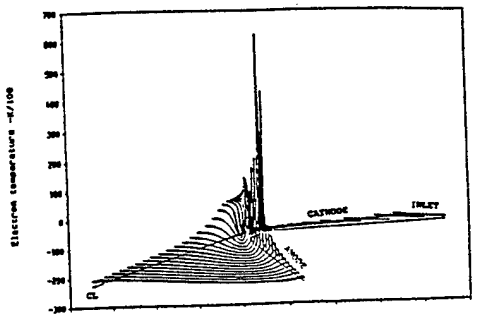

(a)

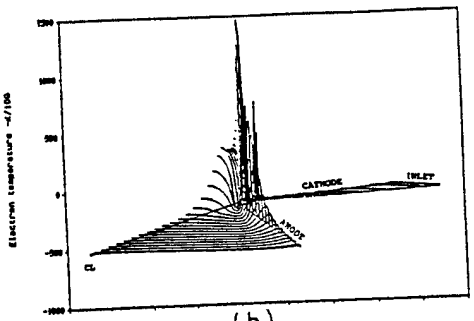

(b)

Figure 15. Calculated electron temperatures. The "fast" chemistry results are shown in (a) and the "slow" chemistry results are shown in (b).

6.2 TT1 Thruster Simulations

A converged solution for the TT1 thruster was obtained for the "slow" chemistry which agrees quite well with the experimental data for this case (Table 4).

The configuration of both these thrusters are the same, except that the TT1 thruster has a contoured nozzle. The conical MARC nozzle was used

Table 4. Comparison of calculated results from the non-equilibrium code using the "slow" reaction rates with experimental data for the TT1 thruster.

	Calculation	Data
Area (m^2)	$.673 \times 10^{-4}$	$.673 \times 10^{-4}$
Mass (kg)	$.100 \times 10^{-3}$	$.100 \times 10^{-3}$
P_{inlet} (Atm.)	0.68	–
Thrust (N)	0.603	0.626
isp (sec)	615.6	638.2
ke (kW)	3431.	–
Efficiency	0.173	0.185
I (A)	61.3	61.3
E (V)	160.	160.
EI (kW)	9.8	9.814
J^2/σ (kW)	9.404	–

for this simulation because the new algorithm used to obtain the zero normal gradient boundary condition for the magnetic field on the anode has not yet been generalized to work for a contoured nozzle. The "fast" chemistry and the equlibrium cases failed to converge for the TT1 case, with the residual errors reaching a stable level with a rather regular oscillation about this level. The failure of the equlibrium case is rather surprising, since the terms which seem most likely to introduce the instabilities do not occur in this case.

6.3 Status of the Computational Code

The UTSI model has been able to provide converged solutions to four out of six cases attempted. Convergance is slow and the residual errors oscillate. It has taken up to 60,000 iterations to obtain a satisfactory solution. This required about 50 hours on a 6 megaflop IBM 320 RISC 6000 machine.

At this point we feel that the algorithm is giving solutions which are trustworthy enough to make some evaluations of the physics included in the model. First, we neglect the excitation energy of the hydrogen atom. Park [22] proposes the assumption that the electronic excitation levels are in equilibrium with the electron temperature. Adopting this assumption would have the effect of increasing the effective electron specific heat and reducing the sensitivity of the electron temperature to variations in energy input. This should make the equations more stable and promote faster convergence. The effect of this change on the ability of the model to predict experimental data is unknown at this time. Second, the ability to predict the correct voltage and power depends on having the correct spatial distribution of the electrical conductivity. There appear to be significant regions in the flow where the gas deviates from an ideal plasma, as determined by the value of log Λ [17]. This occurs where the electron temperature is low and the electron density is relatively high. The points in the converged solution for the MARC thruster with "fast" chemistry where log $\Lambda < 4$ is shown in Fig. 16.

There is a need to develop a proper and efficient method to calculate electrical and thermal conductivities in a non-ideal, non-equilibrium plasma. The electron-ion collision cross-section, which is a major factor in the electrical conductivity, also appears in other transport terms and in the rate at which electrons exchange energy with the heavy species. Modifications to account for plasma non-ideality will have consequences that extend beyond the effects of electrical conductivity. The relative insensitivity of the results to the chemical rates needs to be studied in greater detail to determine if it is a general conclusion or one specific to the cases tested.

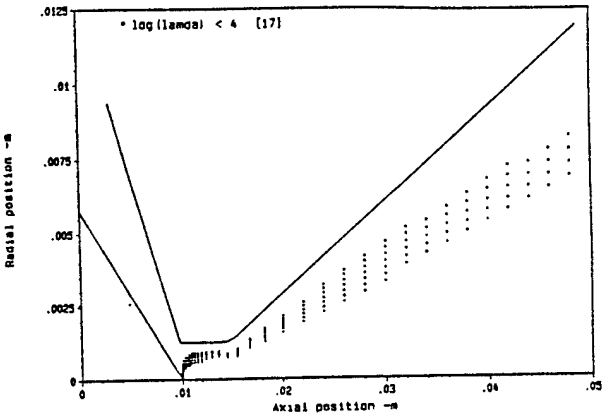

Figure 16. Points in the converged solution for the MARC thruster with "fast" chemistry where log $\Lambda < 4$.

In principal, the UTSI non-equlibrium arcjet model could be applied to arcjets using the hydrogen-nitrogen propellants (ammonia or hydrazine) after a transport and reaction model for this system is developed. In practice, with the more complex system, convergance problems could become worse and the assumption of a single diffusion coefficient for the mixture becomes questionable. If diffusive separation of H and N occurs within the nozzle, it can only be predicted if indivdual species diffusion coefficients are obtained and the equations which use these coefficients are reformulated.

References

1. Jeng, S.-M., Keefer, D. R.,Welle, R., and Peters, C. E., "Laser-Sustained Plasmas in Forced Convective Argon Flow, Part II: Comparison of Numerical Model with Experiment," *AIAA Journal*, Vol. 25, No. 9, pp. 1224-1230, September 1987.
2. Gosman, A. D., and Pun, W. M., "Calculation of Recirculating Flows," Report No. HTS/74/12, Dept. of Mechanical Engineering, Imperial College, London, 1974.
3. Rhie, C. M., "A Pressure Based Navier-Stokes Solver," AIAA-86-0207, AIAA 24th Aerospace Sciences Meeting, Reno, NV, January 1986.
4. Jeng, S.-M., and Keefer, D., "Theoretical Evaluation of Laser-Sustained Plasma Thruster Performance," *Journal of Propulsion and Power*, Vol. 5, No. 5, pp. 577-581, Sept.-Oct. 1989.

5. Rhodes, R. P., and Keefer, D., "Numerical Modeling of a Radio Frequency Plasma in Argon," *AIAA Journal*, Vol. 27, No. 12, December 1989, pp. 1779-1784.

6. Zerkle, D. K., and Krier, H., "On-local Thermodynamic Equilibrium in Laser Sustained Plasmas," AIAA, 23rd Plasmadynamics and Lasers Conference, Nashville, TN, July 1992.

7. Haag, T., and Curran, F. "High Powered Hydrogen Arcjet Performance," AIAA 91-2227, 27th AIAA/SAE/ASME/ASEE Joint Propulsion Conference, Sacramento, CA, June 1991.

8. Moeller, T. M., Keefer, D., and Rhodes, R. P., "Comparison of Experimental and Numerical Results for Radiation-Cooled and Water-Cooled Hydrogen Arcjets," IEPC-93-214, 23rd International Electric Propulsion Conference, Seattle, WA, September 1993.

9. Demtroder, W., Laser Spectroscopy, Springer-Verlag, New York, 1981.

10. Liebeskind, J. G., Hanson, R. K., and Capelli, M. A., "Velocity Measurements in a Hydrogen Arcjet Using LIF," AIAA-91-2112, June 1991.

11. Ruyten, W. M., and Keefer, D., "Two-Beam Multiplexed Laser-Induced Fluorescence Measurements of an Argon Arcjet Plume," *AIAA Journal*, Vol. 31, No. 11, pp. 2083-2089, November 1993.

12. Rhodes, R. P., and Keefer, D., "Non-equilibrium Modeling of Hydrogen Arcjet Thrusters," IEPC-93-217, 23rd International Electric Propulsion Conference,Seattle, WA, September 1993.

13. Rhodes, R. P., and Keefer, D., "Numerical Modeling of an Arcjet Thruster," AIAA 90-2614, 21st International Electric Propulsion Conference, Orlando, FL, June 1990.

14. Ozisik, M. N., "Radiative Transfer and Interactions with Conduction and Convection," John Wiley & Sons, New York, 1973.

15. Rhodes, R. P., and Keefer, D., "Comparisons of Model Calculations with Experimental Data from Hydrogen Arcjets," IEPC 91-111, 22nd International Electric Propulsion Conference, Viareggio, Italy, October 1991.

16. Curran, F. M., and Manzella, D. H., "The Effect of Electrode Configuration on Arcjet Performance," AIAA-89-2722, AIAA/ASME/SAE /ASEE 25th Joint Propulsion Conference, Monterey, CA, July 1989.

17. Zollweg, R. J., Westinghouse Corporation, Computed and supplied the ammonia property tables to UTSI.

18. Zollweg, R. J., and Liberman, R. W., "Electrical Conductivity of Non-ideal Plasmas," *Journal of Applied Physics*, Vol. 62, No. 9, pp. 3621-3627, November 1987.

19. Cho, K. Y., "Non-equilibrium Thermodynamic Models and Applications to Hydrogen Plasmas," Ph.D. Thesis, Georgia Institute of Technology, March 1988.

20. Griem, H. R., "Plasma Spectroscopy," McGraw-Hill Book Co., New York, 1964.

21. Rhodes, R. P., and Keefer, D., "Modeling Arcjet Space Thrusters," AIAA 91-1944, 27th AIAA/SAE/ASME/ASEE Joint Propulsion Conference, Sacramento, CA, June 1991.

22. Park, C., Non-equilibrium Hypersonic Aerothermodynamics, John Wiley & Sons, New York, 1990.

23. Mikatarian, R. R., Kau, C. J., and Pergament, H. S., "A Fast Computer Program for Non-equilibrium Rocket Plume Predictions," AeroChem TP-282, August 1972.

24. Wilke, C. R., "A Viscosity Equation for Gas Mixtures," *J. of Chemical Physics*, Vol. 15, 1950, pp. 517-519.

25. Moeller, T., Rhodes, R. P., Keefer, D., Sedgi-Nasab, A., and Ruyten, W., "Comparison of Experimental and Numerical Results for an Argon Arcjet," AIAA 92-3105, 28th AIAA/SAE/ASME/ASEE Joint Propulsion Conference, Nashville, TN, July 1992.

26. Burtner, D., Keefer, D., and Ruyten, W. M., "Experimental and Numerical Studies of a Low-power Arcjet Opperated on Simulated Ammonia," AIAA-94-2869, 30th Joint Propulsion Conference, Indianapolis, IN, June 1994.

27. Zimmerman, M., and Miles, R. B.,"Hypersonic-Helium-Flow-Field Measurements with the Resonant Doppler Velocimeter," *Applied Physics Letters*, Vol. 37, No. 10, pp. 885-887, 1980.

28. Ruyten, W. M., and Keefer, D., "Absolute Doppler Shift Calibration of Laser Induced Flourescence Signals Using Optogalvanic Measurements in a Hollow Cathode Lamp," *Applied Physics Letters*, Vol. 61, No. 8, pp. 880-882, 1992.

29. Ruyten, W. M., Burtner, D., and Keefer, D., "Spectroscopic Investigation of a Low-Power Arcjet Plume," AIAA paper 93-1790, 29th Joint Propulsion Conference, Monterey, California, June 1993.

30. Ruyten, W. M., Burtner, D., and Keefer, D., "Laser-Induced Fluorescence Measurements on the Plume of a 1 kW Arcjet Operated on Simulated Ammonia," IEPC paper 93-127, 23rd International Electric Propulsion Conference, Seattle, Washington, September 1993.

31. Glocker, B., and Auweter-Kurtz, M., "Radiation-Cooled Medium Power Arcjet Experiments and Thermal Analysis," AIAA-92-3834, 28th Joint Propulsion Conference, Nashville, TN, July 1992.

32. Glocker, B., Auweter-Kurtz, M., Goelz, T. M., and Schrade, H. O., "Medium Power Arcjet Thruster Experiments," AIAA-90-2531, 21st International Electric Propulsion Conference, Orlando, FL, July 1990.

33. Miller, S., and Martinez-Sanchez, M., "Non-equilibrium Numerical simulation of Radiation-Cooled Arcjet Thrusters," IEPC-93-218, 23rd International Electric Propulsion Conference, Seattle, WA, September 1993.

34. McCay, T. D., and Dexter, C. E., "Chemical Kinetic Performance Loss for a Hydrogen Laser Thermal Thruster," *J. Spacecraft and Rockets*, Vol. 24, No. 4, pp. 372-376, 1987.